Master Thesis Report

Erasmus Mundus Joint Master Degree

Surface, Electro, Radiation and Photo-Chemistry (SERP+)

Synthesis of gold nanoparticles encapsulated in fluorinated micelles and evaluation of their radio-sensitizing/radio-amplifying potential on cancer cell cultures

Ngohile Hope Iorav

Supervised by

Professor Erika Porcel

Dr Edmond Gravel

January to July, 2024

FLY LEAF

TABLE OF CONTENT

ACKNOWLEDGEMENTS

I would like to express my profound gratitude to my internship supervisors, Professor Erika Porcel and Dr. Edmond Gravel, for their unwavering guidance and support throughout this remarkable research.

I extend my heartfelt thanks to Professor Sandrine Lacombe, the director of the SERP+ Masters program, for her inspiration and to the coordinators and staff for making these two years of study so enriching and rewarding. Special thanks to Eva Renouf and Vivian for simplifying the administrative processes with their valuable information.

I am deeply appreciative of the European Commission for funding my Master's studies and the CNRS for supporting this internship. My sincere thanks to Foutina Feghali and Mathilde Ponchelle for their availability and willingness to guide me in the lab.

I am also grateful to my home country professors, Dr. Ungwanen Ahile and Dr. Joseph Gbertyo, for their immense support and inspiration throughout my studies.

Finally, a special thank you to my friends and family for their continuous support, especially my husband Ngutor Emmanuel Chagbe and our son Othniel Ternamdoo Chagbe, for their unwavering support during this time.

Abstract

Cancer is the second leading cause of death world wide and most patients receive radiotherapy in the course of their treatment. While radiotherapy presents the advantage of targeting deeply sited tumors, it suffers from tumor radioresistance, induced by different mechanisms and most importantly hypoxia. Tumour hypoxia is a condition where tumour cells are deprived of oxygen supply, thus rendering ionizing radiation ineffective. This is because, a lack of oxygen limits the generation of reactive species which are responsible for tumour cell damage. Perfluorinated micelles can solubilize 20 times more oxygen than water and have been employed to alleviate hypoxia in tumour cells. This work aims to design a nanocarrier where gold nanoparticles (AuNPs) are encapsulated within perfluorinated micelles (PFTD-PEG) and to evaluate the radiosensitisation/radioamplification potential of this nanoparticle (NP). A synergistic effect is envisioned, with fluorinated micelles to sensitise the tumour, by delivering oxygen and AuNPs to amplify the effect of radiation by electron generation. The nanocarrier was characterized using UV-Vis spectroscopy, DLS and TEM. By clonogenic assay, the toxicity of this NP was accessed and the results showed that although perfluorinated micelle was not toxic, the AuNP@micelle composite was toxic to cells as only 34 % of cells survived after exposition . To evaluate the potential synergistic effect between perfluorinated micelles and high Z metal NPs, B16F10 cells were irradiated after incubation with non-toxic platinium (Pt) NPs plus perfluorinated micelles. The results were encouraging, as more cell death was noticed in the cells incubated with both PtNPs and PFTD-PEG micelles, compared to cells incubated with either Pt NPs or PFTD-PEG micelles. This result proves the additive effect of PFTD-PEG micelles and high Z metal NPs in enhancing the effect of radiation.

Résumé

Le cancer est la deuxième cause de mortalité dans le monde et la plupart des patients reçoivent une radiothérapie au cours de leur traitement. Si la radiothérapie présente l'avantage de cibler les tumeurs situées en profondeur, elle reste en échec face à la radiorésistance des tumeurs, induite par différents mécanismes, dont le plus important est l'hypoxie. L'hypoxie tumorale est un état dans lequel les cellules tumorales sont privées d'oxygène, ce qui rend les rayonnements ionisants inefficaces. En effet, le manque d'oxygène limite la production d'espèces réactives responsables de la détérioration des cellules tumorales. Les micelles perfluorées peuvent solubiliser 20 fois plus d'oxygène que l'eau et ont été utilisées pour réduire l'hypoxie dans les cellules tumorales. Ce travail vise à concevoir un nanocarrier dans lequel des nanoparticules d'or (AuNP) sont encapsulées dans des micelles perfluorées et à évaluer le potentiel de radiosensibilisation/radioamplification de ces nanoparticules (NP). Lors de la radiothérapie et de l'utilisation combinée de la micelles pour sensibiliser la tumeur en délivrant de l'oxygène, et des AuNP pour amplifier l'effet du rayonnement par la génération d'électrons, un effet synergique est envisagé. Le nanocarrier a été caractérisé par spectroscopie UV-Vis, DLS et TEM. La toxicité de cette NP a été évaluée par un test clonogénique et les résultats ont montré que bien que les micelles perfluorées ne soient pas toxiques, le composite micelle/AuNP était toxique pour les cellules, puisque seulement 34 % d'entre elles ont survécu après l'exposition. Afin d'évaluer l'effet synergique potentiel entre la micelle perfluorées et les NP métalliques à haute teneur en *Z*, des cellules B16F10 ont été irradiées après avoir été incubées avec des NP de platine (Pt) non toxiques et des micelles perfluorées. Les résultats sont encourageants, car la mort cellulaire est plus importante dans les cellules incubées à la fois avec des NP de Pt et des micelles perfluorées que dans les cellules incubées avec des NP de Pt seules ou des micelles seules. Ce résultat prouve l'effet synergique de la micelle PFTD-PEG et des NP métalliques à Z élevé dans l'amélioration de l'effet des radiations.

LIST OF ABBREVIATIONS

Z - Atomic number
E - Photon energy
ɵ - Theta
ϕ - Phi
e^- - Electron
e^+ - Positron
DNA - Deoxyribonucleic acid
HIF - hypoxia-induced factor
PFC - Perfluorinated Carbon
MRI - Magnetic resonance imaging
PET - Positron emission tomography
ISMO - Institute of molecular sciences of orsay
CEA - Atomic energy commission
AuNP - Gold nanoparticle
PtNP - Platinum nanoparticle
PEG - Poly(ethylene) glycol
PFTD-PEG - perfluorotetradecanol-poly(ethylene) glycol
CH_2Cl_2 - Dichloromethane (DCM)
Et_3N - Triethylamine
Et_2O - Diethyl ether
$MgSO_4$ - Magnesium sulphate
THF - Tetrahydrofuran
$HAuCl_4.3H_2O$ - Chloroauric acid trihydrate
FBS - Fetal bovine serum
NaH - Sodium hydride
NMR - Nuclear magnetic resonance
DLS - Dynamic light scattering
TEM - Transition electron microscopy
TOAB - Tetraoctylammonium bromide
PFMC - Perfluoro methylcyclohexane
PFSH - 1H, 1H, 2H, 2H perfluorodecanethiol
CMC - Critical micelle concentration
DMEM - Dulbecco’s modified eagles medium
PBS - Phosphate buffer saline
P/S - Penicillin streptomycin
FBS - Fetal bovine serum
PFA - Paraformaldehyde
PE - Plating efficiency
ESI-MS - Electrospray ionisation mass spectrometry
$NaHCO_3$ - Sodium hydrogen carbonate
RBE - Relative biological effectiveness
RT - Room temperature

1 INTRODUCTION

1.1 What Is Radiotherapy

Radiotherapy, also known as radiation therapy, is a treatment modality for solid tumours that employs ionizing radiation to damage cancer cells, thereby stopping their growth and proliferation[1,2]. Cancer generally refers to diseases that cause genetic changes to cells of the body, undergoing metastasis (in some cases) and spreading to other parts of the body[3]. Cancer has been identified as one of the leading causes of death worldwide, with 19.3 million new cases and 10 million deaths in 2020[4]. About 60 - 65% of cancer patients worldwide receive radiotherapy either as a stand-alone treatment[5], particularly in the case of early tumours, or in combination with other treatments, such as surgery, immunotherapy and chemotherapy[2]. The conventional ionizing radiation used in radiotherapy are high energy photons (γ-rays or x-rays, MeV range). These photons present the advantage of deep tissue penetration, thereby reaching deeply sited tumours, even up to 10cm deep[6]. It is worth noting that Wilhelm Röntgen discovered X-rays in late 1895, which marked the beginning of radiotherapy[7], thus earning him the first Nobel prize in physics. When γ-rays or x-rays pass through a sample, there is an interaction between the photon and the medium, resulting in energy transfer to the medium. This interaction between the radiation and medium produces three major effects: photo-electric effect, Compton effect and pair production[5] (Figure 1). Photo-electric effect dominates at low energies, while pair production is more prevalent at high energies, however, at the energy of radiation, the most important interaction is the Compton effect[8].

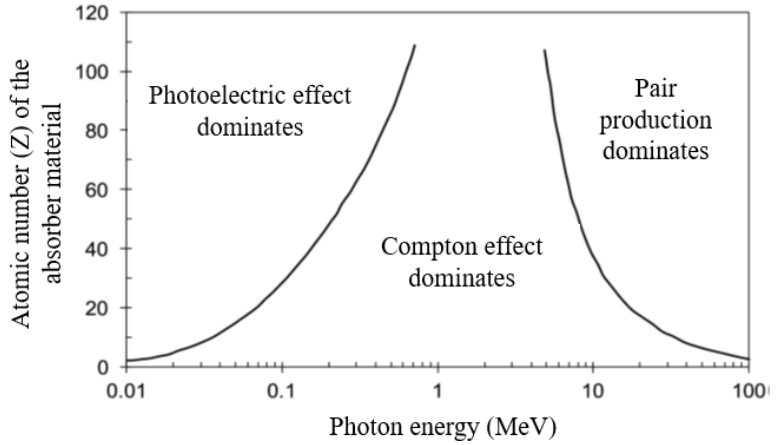

Figure 1a. The relative significance of the primary photon interactions in relation to atomic number (*Z*) and photon energy (Adapted from Laprise-Pelletier *et al*) [9].

During photoelectric effect, the photon interacts and transfers its energy to an inner shell electron. Part of the energy is used to overcome the electron's binding energy and the remaining is translated into the kinetic energy of the photo-electron as it escapes the nucleus. The dependence of photoelectric effect on the atomic number (*Z*) of the atom and photon energy (E) is Z^5 and E^{-3}, respectively[8]. Compton effect dominates in the energy range between 0.1 and 10 MeV. During Compton process (Figure 1b), a high-energy photon interacts and transfers part of its energy to electrons (in the medium), thereby scattering the electrons at an angle ɵ. Due to this interaction and loss in energy, the photon is also scattered at an angle ϕ and as a result undergoes a change in wavelength[5]. Compton interaction is independent of *Z* and decreases with increasing photon energy[8]. In pair production, the photon interacts and transfers all its energy to the nucleus, producing an electron (e^-) and a positron (e^+). This interaction occurs only if the photon energy is greater than 1.02 MeV[8].

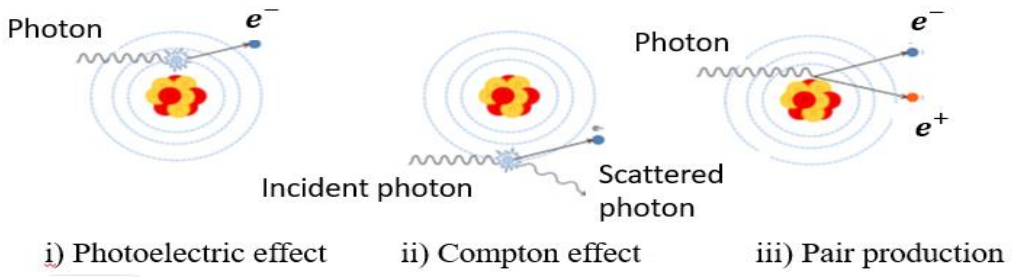

Figure 1b. The major interactions in radiation energy (Adapted from Mott *et al*)[8].

In the case of biological media, the released electrons either cause direct damage to biomolecules such as Deoxyribonucleic acid (DNA) or react with surrounding water molecules to produce reactive species (a process known as water radiolysis) and in particular, reactive oxygen species (ROS) that cause indirect damage[10] (Figure 2).

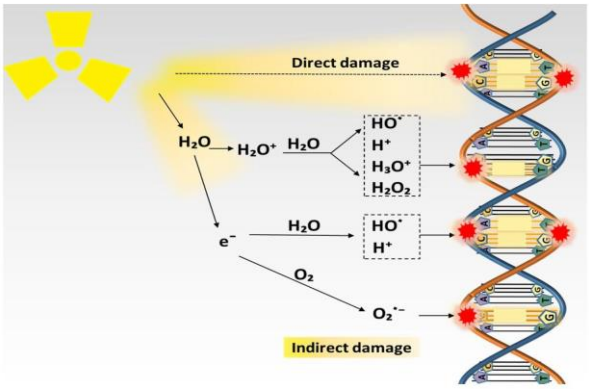

Figure 2. Direct and indirect damage caused by ionizing radiation (Adapted from Wang *et al*)[10].

In recent times, the use of ion beams have become prevalent and shows promising results[6]. Ion beams present the advantage of more efficient targeting and delivery of a high radiation dose to the targeted region while minimising the dose elsewhere, thanks to the bragg peak. This gives rise to an increase in the relative biological effectiveness (RBE) of radiation to values around 3[11].

Due to the functional mechanism in healthy cells, they can survive DNA damage better (although a fraction of them also die), repairing even damages between two irradiation doses. On the other hand, cancer cells can scarcely repair these damages due to their defective mechanisms, and this advantage of healthy cells over tumour cells gives radiotherapy its therapeutic window[2]. It should be noted that the tumour damage caused by these ionizing radiations comes with side effects, such as damage to healthy nearby tissues, vasculature and nerves; and neoplastic changes sometimes resulting in secondary tumours. This disease reoccurrence could eventually lead to clinical radioresistance. Other factors that induce resistance in radiotherapy are the inherent mechanisms of cancer cells (such as mutation and genetic specificities)[12] and most especially hypoxia[13].

1.2 Effect of hypoxia in Radiotherapy

Hypoxia refers to a decrease in oxygen supply at the tissue level in the body, which leads to cellular dysfunction. Different conditions can lead to hypoxia: decrease in oxygen supply, increase in oxygen consumption, or abnormal use by cells, which leads to an imbalance in its supply and consumption[14]. In hypoxic conditions, tumours can shift their metabolism from aerobic to anaerobic energy production pathways to adjust to the O_2^- depleted environment by activating the hypoxia-induced factor (HIF)[13]. Two types of hypoxia exist in solid tumours (Figure 3), these include acute and chronic hypoxia. Acute hypoxia occurs when blood vessels are narrowed, giving rise to an alteration in blood supply. Chronic hypoxia (diffusion limited) is experienced when there is a limitation in diffusion of oxygen from tumour microvessels to nearby tissues[15].

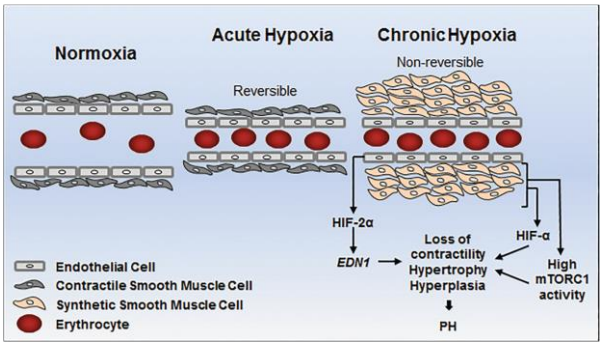

Figure 3. Acute and chronic hypoxia (Adapted from Charolidi *et al*)[16].

Crabtree et al. studied some factors that influenced the susceptibility of cancer cells to an X-ray source (radium). Their findings revealed that cells were much more sensitive to X-rays in the presence of oxygen. In fact, tumour cells in hypoxic regions survived radiation three times more, compared to tumour cells in aerobic regions[15]. Thus, it can be said that oxygen is a key determinant of cellular response to ionizing radiation, and its absence (hypoxia) gives rise to 3 times radioresistance[10]. To explain this phenomenon, the oxygen fixation hypothesis (Figure 4) is proposed. Under aerobic conditions, radiation induces ionization and subsequent production of radicals in the vicinity of DNA. These radicals then react with oxygen, causing permanent DNA damage (double-strand breaks). When oxygen is absent (hypoxic condition), the radicals are reduced to the original form and permanent DNA damage is hindered[10].

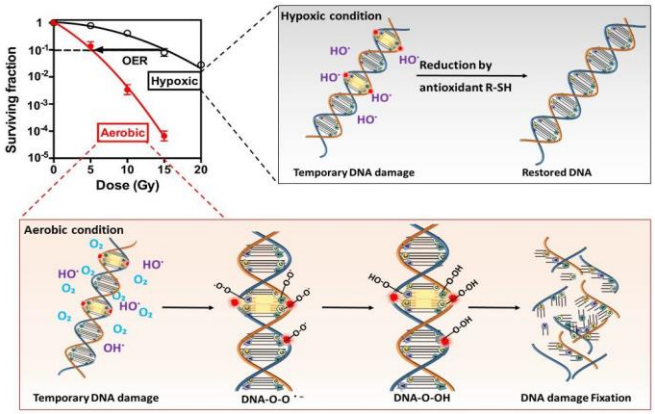

Figure 4. Effect of hypoxic and aerobic conditions on survival fraction (Oxygen fixation hypothesis) (Adapted from Wang *et al*)[10].

Hypoxia induces an increase in tumor metastasis and malignancy potential[15] and is a major limitation to many cancer treatments, including chemotherapy, immunotherapy and radiotherapy[17]. Additionally, hypoxia gives immunosuppressive properties to the tumour microenvironment so that the immune system does not notice the tumour[18]. Since radiotherapy highly depends on oxygen availability, there is a crucial need for hypoxic radiosensitizers[10] to assist in alleviating tumour hypoxia.

Studies are in progress, seeking ways to combat tumour radioresistance induced by hypoxia. Strategies such as oxygen-mimetic nitroimidazoles and hyperbaric oxygenation exist[10] and have demonstrated significant local tumour control. However, they are not yet in clinical practice due to their neurotoxicity. Approaches such as inhibition of antioxidant enzymes, HIF-1 and tumour metabolism have also been considered[10]. Furthermore, oxygen carriers based on perfluorinated carbons (PFCs) have been used to deliver oxygen to tumours and improve cancer therapies[13]. For example, hypoxia-induced radioresistance was alleviated in a brain tumour in mice using an oxygent-based nanoemulsion (a PFC nanoemulsion)[19].

1.3 Perfluorinated Carbons (PFCs)

PFC colloids have been studied to enhance oxygen delivery in nanomedicine including microbubbles, nanoemulsions[17] and phase shift nanoemulsions[20]. Some properties of PFCs that make them good therapeutic candidates include their high gas solubility and transport ability[21], chemical inertness, hydrophobicity and lipophobicity, thermal stability[22], and their self-segregation potential[17]. Since they are both lipophobic and hydrophobic, PFC colloids tend to keep to themselves, neither mixing in lipids nor aqueous phases. This property enables their proper circulation *in vivo* for a reasonable period, which is necessary for imaging experiments[21]. Their stability is due to poor water solubility and high volatility (because of low intermolecular forces). PFCs can dissolve 20 times more oxygen compared to water, thus making them excellent oxygen carriers[17]. This is because of the very low polarizability of fluorine atoms, giving rise to limited van der Waals forces between PFC molecules. Since these van der Waals intermolecular forces are weak, this makes PFCs behave like ideal gas-like fluids, dissolving other gases of similar cohesivity, such as CO_2 and O_2. Many PFCs are used to design fluorinated colloids for medical applications (Figure 5), with linear PFCs solubilising more oxygen than cyclic ones[17].

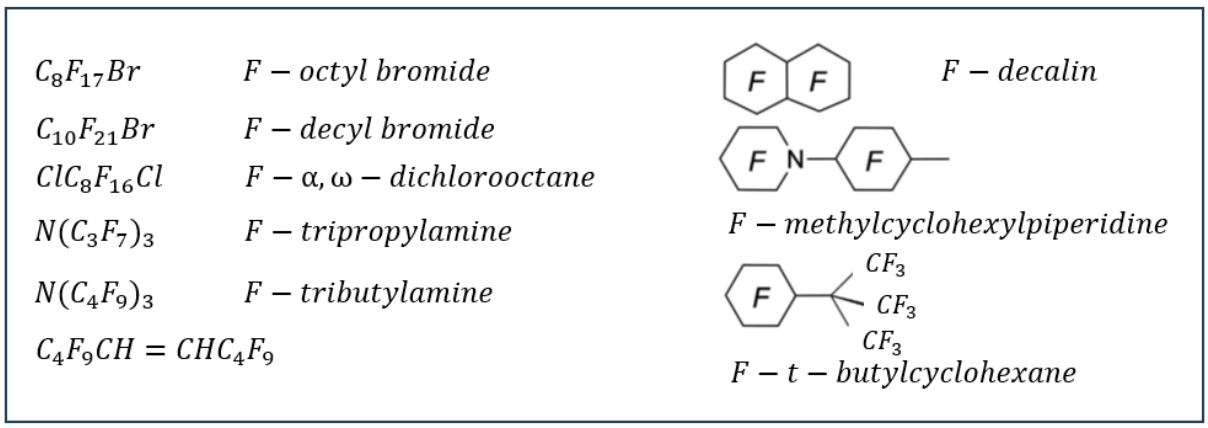

Figure 5. PFCs used in perfluorinated colloid design for medical applications (Adapted from Krafft *et al*)[17]

Previous works from the literature report the loading of PFCs within nanomaterials such as paramagnetic Fe_3O_4 NPs[23] and gold nanoshells[24]. Recent studies showed that F-pentane loaded with ^{64}Cu-labeled organosilica NPs alleviated hypoxia and enhanced radiotherapy[25]. Song et al. also reported the oxygen transport capacity of Perfluoro hexane loaded within hollow Bi_2Se_3 NPs, and the ability of this particle to fight hypoxia-induced tumour radioresistance in mice[26]. Building on these promising developments on the potential of perfluorinated colloids in nanomedicine, the CEA team conducted research on PFTD-PEG micelles to evaluate their ability to reduce hypoxia in mouse melanoma and enhance the effect of radiation. The results showed that the micelles alone were not toxic to the cells, but in the presence of radiation, the micelles increased the effect of gamma rays, achieving a sensitizer enhancement ratio of 1.23[27]. Micelles can solubilize hydrophobic drugs and ensure their biocompatibility. Their small size enables blood circulation and subsequent accumulation in the desired region[28]. These properties, therefore, make them promising nanocarriers.
Interestingly, the roles of PFCs are not limited to oxygen delivery. They have also demonstrated potential in magnetic resonance imaging (MRI)[29] and positron electron temography (PET)[27] imaging, thereby showing promise as a theranostic tool. In general, colloids made of perfluorinated carbons can be loaded with drugs, markers, and nanoparticles, enabling selective release of the particle at the desired site, thus minimizing side effects to healthy tissues[17].

1.4 Metallic Nanoparticles

Although higher doses of radiation can produce better tumour control (particularly in hypoxic regions), the dosage which can be given is limited by the possibility of normal tissue damage[5]. Therefore, current strategies are under development aimed at improving radiotherapy outcomes. These include minibeam irradiation, heavy-ion irradiation, spatial and time dose fractionation[30]. The use of radio-enhancers to improve selectivity[31] and amplify the effect of radiation while maintaining a safe and therapeutic dose[32] is also explored. High *Z* metal nanoparticles have been widely studied as promising radioenhancers. A pool of secondary electrons is produced after the activation of high Z metal nanoparticles by irradiation. These electrons then react with water and molecular oxygen to generate additional reactive species responsible for biomolecular damage and, therefore, cancer cell killing. Hainfeld *et al*. first demonstrated the radioenhancement potential of gold nanoparticles (AuNPs) in mouse carcinoma. They found that AuNPs were not toxic to the mouse and were safely excreted through the kidney[33]. This finding laid the foundation for other interesting studies on AuNPs and high *Z* metals in general. Gold nanoparticles are biocompatible[34] and have a high atomic number, with high density, variable size and a surface for easy attachment of ligands. These properties makes them good candidates for imaging[35] and enhancers of radiotherapy[36].

Several other promising metal nanoparticles have been studied, including, but not limited to, platinum, gadolinium, iron and hafnium[29]. Since nanoparticles have a large surface area and are easy to modify in terms of size, shape and charge[32], these properties make them good candidates for a wide range of clinical applications such as imaging, photosensitizers, drug delivery molecules, vaccine adjuvants and radiation dose enhancers[35]. Hafnium is at phase 2-3 and gadolinium at phase 1 of clinical trials[32].

Li et al reported the radioenhancing potential of PtNPs on Deinococcus radiodurans (a highly radioresistant bacterium). They internalized PtNPs into the cells and irradiated them using a gamma source. The result showed a radio amplification of more than 40%

in the presence of the NP[37]. It is worth noting that the group of ISMO patented a platinum NP with radioenhancing properties. They were the first to demonstrate the sensitising properties of PtNP in comparison with other metal atoms. They found that PtNPs significantly enhanced the effect of radiation, showing a sensitiser factor of 1.4 and 2.1 for single and double strand breaks in DNA respectively[38]. Salado et al. also demonstrated that bimetallic Au:Pt-PEG NPs increased the production of double-strand breaks (lethal damage) in plasmid DNA by 90 %[36]. This radio enhancement effect is expected to target the tumour while sparing the normal tissue, and this is made possible by the enhanced permeability and retention (EPR) effect in tumour tissues (Figure 6). Tumour cells multiply rapidly, placing a high demand on oxygen and nutrient supply. To meet this oxygen demand, the tumour vasculature (the network of blood vessels, responsible for oxygen and nutrient supply) grows abnormally, such that the endothelial cells are poorly aligned with gaps between them. This structural anomaly, coupled with the production of substances such as nitric oxide and vascular endothelial growth factor, makes the tumour's blood vessels permeable. The rapidly growing tumour also collapses the lymph vessels, giving rise to poor lymphatic drainage. The nanoparticles, therefore, leverage the tumour's poor lymphatic drainage and enhanced permeability to preferentially go into the tumour and accumulate there[28].

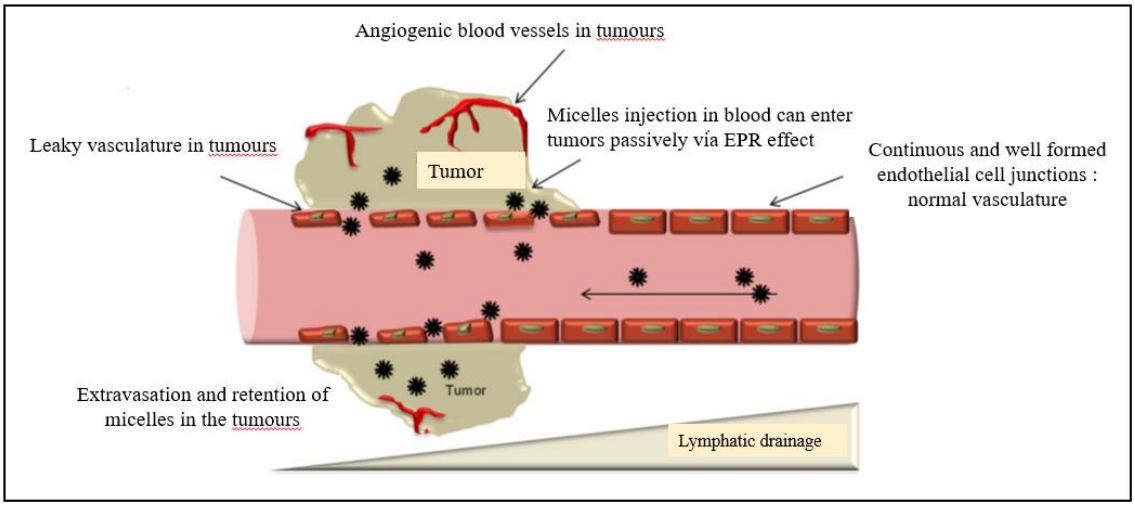

Figure 6. Enhanced Permeability and Retention (EPR) effect (Adapted from Jhaveri *et al*)[28]

1.5 Aims and objectives Of The Study

Through her PhD thesis work, Sophia Godel-Pastre has demonstrated the radiosensitisation potential of PFTD-PEG micelles, owing to their ability to solubilise oxygen and transport it to the tumour site[27]. On the other hand, extensive studies on AuNPs have proven their ability to amplify the effect of radiation by generating a cascade of electrons, which in turn produces reactive species that cause damage to the tumour[10]. Therefore, this project aims to encapsulate AuNPs within PFTD-PEG micelles and evaluate their combined therapeutic potential on cancer cell cultures. This particle, AuNP@PFTD-PEG is envisioned to play the dual role of radiosensitisation/ radioamplification, thereby achieving a synergistic effect.

2. MATERIALS AND METHODS.

2.1 Synthesis of PFTD-PEG amphiphile and their assembly into micelle.

2.1.1 Synthesis of Tosylated PEG. In a 100 mL round bottom flask under inert atmosphere, PEG monomethylether (MW = 2000, 3.15g, 1.6 mmol, 1 equiv.) was dissolved in dry dichloromethane (CH_2Cl_2, DCM, 31.5 mL). Then Triethylamine (Et_3N, 0.79 g, 7.9 mmol, 5 equiv.) was added, followed by a dropwise addition of Tosyl chloride (TosCl, 1.50g, 7.9 mmol, 5 equiv.) and the solution was stirred at room temperature (RT) overnight. After completion, the reaction mixture was treated with water and brine and the aqueous phase was extracted with DCM. The organic layer was then dried over magnesium sulphate ($MgSO_4$) and concentrated under vacuum. The product was purified by precipitation with Diethyl ether (Et_2O) at −20 °C for 2 h. The mixture was filtrated to obtain the expected product as a white solid (3.16g, 1.5 mmol, 93%).

2.1.2 Synthesis of PFTD-PEG amphiphile. Under inert atmosphere, sodium hydride (NaH, 0.11 g, 2.8 mmol, 4 equiv.) in tetrahydrofuran (THF, 7 mL) was slowly added to perfluorotetradecanol (PFTD, 1.46 g, 2.1 mmol, 3 equiv.) in THF (17 mL). The reaction mixture was stirred at reflux (70 ºC) for 30 min, before the tosylated PEG-2000 (1.58 g, 0.75 mmol, 1 equiv.) was added. Thereafter, the reaction mixture was stirred at 70 °C for four days. The reaction was monitored by Nuclear Magnetic Resonance (^{1}H-NMR) and after completion (when there were no more traces of the tosylated starting material), the reaction mixture was cooled to room temperature and THF evaporated. The residual oil (crude product) was solubilised in CH_2Cl_2 and filtered over celite to remove any PFTD left. The filtrate was purified by precipitation with Et_2O at −20 °C for 2 h and PFTD-PEG amphiphile (1.28 g, 0.48 mmol, 68%) was obtained as a white solid.

2.1.3 Assembly of PFTD-PEG amphiphile into PFTD-PEG micelle. To achieve a final micelle concentration of 10 mg mL^{-1}, PFTD-PEG amphiphile (20 mg) was added to ultrapure water (2 mL). This mixture was sonicated for 15 mins using an ultrasonic probe (Branson 550 sonifier) at 40 % power output and a pulse rate of 300 ms pulse per second. After 15 min, the PFTD-PEG micelle was obtained. Sonication helped to homogenise the micelle solution and ensure its stability.

2.2 Gold nanoparticle synthesis

AuNP was synthesised following the modified version of Brust-Schiffrin method. In a 50 mL round bottom flask, a solution of chloroauric acid trihydrate ($HAuCl_4.3H_2O$, 29.5 mg, 0.075 mmol, 1 equiv.) was prepared in extra pure water (2.5 mL). A solution of excess Tetraoctylammonium bromide (TOAB, 192.6 mg, 0.353 mmol, 4.7 equiv.) in toluene was added to form a biphasic mixture. The two-phase mixture was stirred vigorously for 20 mins to achieve a phase transfer of the gold from the aqueous to the organic (toluene) phase. Once completed, a solution of sodium borohydride ($NaBH_4$) in cold extra pure water was prepared and added to the solution. A colour change was observed, from orange to yellow, then green and finally dark red / burgundy, which signified the evolution of the oxidation state of gold from Au (III) to Au (0). The solution was stirred for another 3 h at RT to ensure complete reduction of the gold. Afterwards, the toluene phase was separated from the aqueous phase and 1H, 1H, 2H, 2H-perfluorinated thiol (PFSH, 7 µL) was added, which induced an instant precipitation of the AuNP. Thereafter, the crude mixture was transferred into 7 eppendorf tubes (1 mL each) for the successive washing and centrifugation steps (at least 6 rounds of washing with toluene) with ultrasonication to remove any TOAB. A black precipitate was obtained and after drying the solid under vacuum for 1h, the compound was dissolved in 0.5 mL of perfluoromethylcyclohexane

(PFMC) to get a colloidal suspension of AuNP@PFSH. The perfluorinated thiol ligand, PFSH served to stabilise the AuNP and prevent aggregation

2.3 Encapsulation of AuNPs and Did dye inside the micelle (PFTD-PEG)

2.3.1 Loading of the micelle with AuNPs. AuNP@PFSH (0.5 mL) dissolved in PFMC was added to perfluorinated micellar suspension (PFTD-PEG, 2 mL) in ultrapure water and the two-phase mixture was sonicated with an ultrasonic probe (300 ms pulse per second, power output 40 %) for 6 min. This step was repeated twice, to achieve a total of 3 sonications, with one hour resting period between each sonication. Once complete, the colloidal solution was filtered on a 0.45µm nylon filter and perfluorinated gold nanoparticles encapsulated in PFTD-PEG micelles (AuNp@PFTD-PEG) were obtained.

2.3.2 Loading of the micelle (PFTD-PEG) with AuNPs and Did dye. The encapsulation of PFTD-PEG with AuNPs and Did dye was done in two steps. First, Did dye (8 µL, 1%) was added to PFTD-PEG micelle (2 mL, 10 mg mL^{-1}) followed by sonication with an ultrasonic probe (300 ms pulse per second, power output 40%) for 15 min. Thereafter, AuNP@PFSH (0.5 mL) was added to the colloidal solution and a second sonication was carried out using the same parameters as in the first case. Once complete, PFTD-PEG micelles, encapsulated with gold nanoparticles and Did dye (AuNPDid@PFTD-PEG) were obtained for confocal microscopy experiments. UV-Vis measurements were carried out to confirm the encapsulation of AuNPs and Did dye in the PFTD-PEG micelle, and absorptions at 520 and 633nm were observed for AuNPs and Did dye respectively.

2.4 Platinum nanoparticle (PtNP). AuNP@PFTD-PEG was envisioned to produce a synergistic effect, where the micelle transports more oxygen to the tumour site, thus alleviating hypoxia and radiosensitising the tumour, while the AuNP generates more electrons at the tumour environment to amplify the effect of radiation. Cells were also incubated with already prepared PtNP to compare and prove the synergistic effect of AuNP@PFTD-PEG.

2.5 Characterization of PFTD-PEG micelle and AuNP@PFTD-PEG

2.5.1 Determination of the Critical Micelle Concentration (CMC). To evaluate the concentration at which PFTD-PEG amphiphile began to aggregate into PFTD-PEG micelles, surface tension measurements were carried out using the Du Noüy-Padday method, thanks to the tensiometer (Aqua pi plus). Different solution concentrations of PFTD-PEG amphiphiles in water were prepared, ranging from 0.01 to 1 mg mL^{-1}. First, the Du Noüy ring was sterilised using a welding touch, followed by calibration with air and water to obtain a surface tension of 0 mN m^{-1}. Samples in the container were placed on the measurement stage, and data was acquired on the computer. This method leveraged the interaction between the ring and the liquid surface. After immersing the ring in the sample, the stage was gradually lowered and the ring pulled up the meniscus of the liquid, exerting a force. This force continued to increase until the meniscus tore from the ring. By calculating this maximum force, the surface tension was measured. The software made all the calculations and generated the surface tension values. Three measurements were taken for each sample and surface tension was plotted as a function of the concentration. Two straight lines were obtained, and their point of intersection was estimated as the CMC.

2.5.2 Dynamic Light Scattering (DLS). For the size characterization of PFTD-PEG micelle and AuNP@PFTD-PEG, DLS (VascoFlex instrument from Cordouan Technologies, laser diode at $\lambda = 450$ nm, 25°C, Figure 7) was used. In each case, the

sample was first filtered to get rid of aggregates and 600 µL of sample was transferred to a 1 mL cuvette and placed in the sample holder. The sample area was securely covered before the laser was turned on. The Brownian motion of particles in suspension caused laser light to be scattered in different directions and at different intensities. These intensities (collected by the detector at a known angle) were analysed to give the velocity of the Brownian motion, and using the Stokes-Einstein equation (Equation 1), the size of the particles was determined.

$$\emptyset_H = \frac{kT}{3\pi\mu D} \qquad (1)$$

$\emptyset_H$= hydrodynamic radius, k=Boltzmann constant, T=temperature of the solvent, µ= solvent viscosity, D=diffusion coefficient.

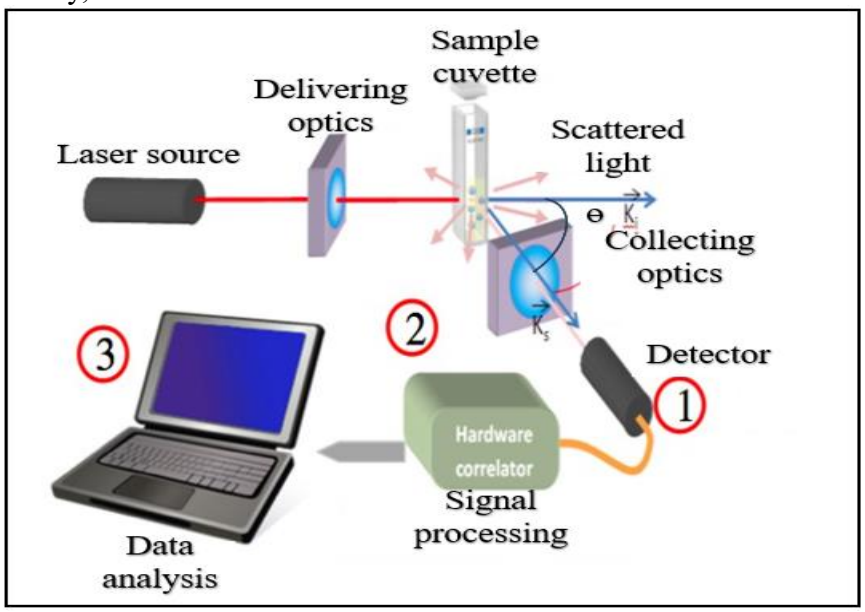

Figure 7. Dynamic Light Scattering (Adapted from Cordouan-tech)[39]

2.5.3 Transition Electron Microscopy (TEM). The size of AuNPs was estimated using TEM (TECNAI 20 G2 FEI, Figure 8). This microscopy leverages the interaction of electrons with the sample to generate an image. To prepare the sample for TEM analysis, AuNP@PFTD-PEG solution was diluted, and a drop of the diluted solution was placed on a TEM copper grid and allowed to dry. Afterwards, the TEM grid was carefully transferred to the sample holder, which was partially inserted in the middle of the column and maintained under vacuum. After 2 min of "pre-vacuum" pumping, the sample holder was completely inserted and turned anti-clockwise, as far as it could go. To produce the image, TEM used high voltage electron beam (200 kV, generated from an electron gun, aligned from top to bottom). The diaphragm capacitor (C2) controlled the electron beam size that travelled through the vacuum. The deflection coils placed at different positions aligned the electron beam at the source and the image. The condenser lenses (which are magnetic) focused the electron beam on the ultra-thin sample so that the electrons interacted with the sample as the beam passed through to generate an image. The electrons scattered by the sample (unwanted electrons) were removed by the objective aperture, while those transmitted by the sample were mapped into an image, magnified (by the lens) and visualised by the detector.

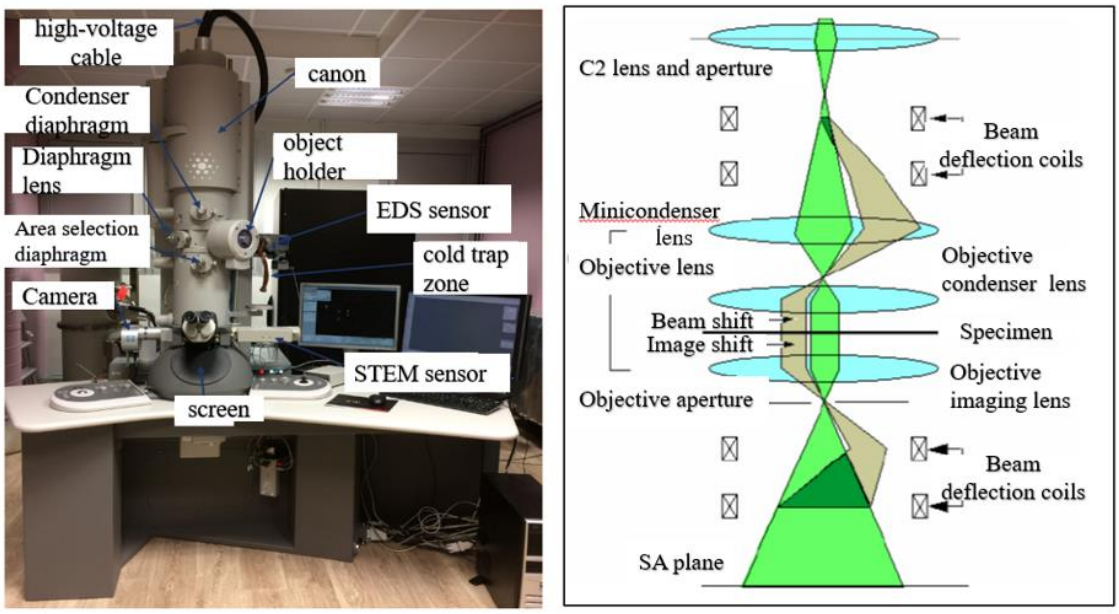

Figure 8. a) Transmission Electron Microscopy (TEM) b) Scheme of the principle of TEM (Adapted from CEA document)[40]

2.6 In vitro analysis of AuNP@PFTD-PEG

2.6.1 Cell culture on B16F10 cell line. B16F10 cell line was used for the experiments. Cells were cultured in Dulbecco's modified eagles medium (DMEM) with glutamax and supplemented with 1% penicillin-streptomycin (P/S) and 10% fetal bovine serum (FBS). Cells were grown in a humidified incubator at 37 °C and 5 to 10 % CO_2 to mimic biological conditions, thus making the environment conducive for them to thrive.

2.6.2 Confocal microscopy. To track the internalisation of the NP *in vivo*, confocal microscopy was carried out using a confocal laser scanning microscope (confocal SP5 Leica). Glass coverslips were first cleaned using plasma cleaner and placed in 6 well plates. B16F10 cells (in T75 flask) were trypsinated and counted using Luna, after which a density of 1.5 10^4 cells was seeded on the coverslips (with culture medium) and placed in the incubator for 24 h, allowing enough time for cell plating. Once complete, cells were incubated with the fluorescently labelled particle (0.25 mg mL^{-1} AuNPDid@PFTD-PEG solution in medium) for 24 h. After this treatment, the medium was discarded and cells were washed with PBS (3 times). To fix the cells, paraformaldehyde (PFA, I mL, 4%) was added in each well containing the cells for 20 min. Cells were rinsed with PBS, stained with Dapi dye (1 µM) for 20 mins and rinsed again with PBS. The coverslips were removed from the well plates with the help of a forcep and carefully placed on a glass slide for confocal imaging.

The glass slide was securely placed on the microscope sample stage and the sample was focused on the objective lens. As confocal microscopy works by the principle of point illumination (Figure 9), only the part of the sample focused on the objective was detected. The fluorophores in the sample (Dapi, λ_{ex}=359nm and Did, λ_{ex}=633nm) were excited by the laser and the first pinhole focused the light beam on the area of interest in the sample. Dapi and Did emitted fluorescence at 457 and 663 nm wavelengths respectively. The fluorescent light was filtered by the dichroic mirror and filter. With the help of a second pinhole positioned in the focal plane, only the light coming from the targeted point of the sample was selected. The surface of the sample was scanned and the fluorescence

(recorded by the detector) was mapped into a 2D image of the sample. With this fluorescence emission, the location of AuNpDid@PFTD-PEG particle inside the cell was monitored.

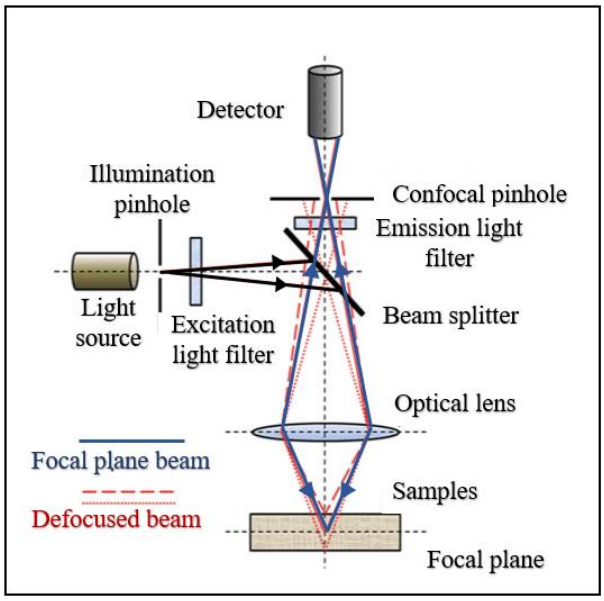

Figure 9. Scheme explaining the principle of confocal microscopy (Adapted from ebrary.net)[41].

2.6.3 Toxicity test (Clonogenic assay). To evaluate the toxicity level of AuNP@PFTD-PEG solution on the cells, clonogenic assay was carried out. In a T25 flask, B16F10 cells were seeded at 10^5 cells mL^{-1} and placed in the incubator at 37 °C in a humidified 5% CO_2 atmosphere 24 h prior to the experiment, allowing enough time for cells to plate in the flask. AuNP@PFTD-PEG solution (10 mg mL^{-1}) was diluted in complete medium to obtain different concentrations ranging from 0.1 to 1 mg mL^{-1}. When incubation was complete, the medium was removed and cells were incubated for 24 h with the different dilute concentrations of AuNP@PFTD-PEG solution. Once complete, the medium was removed, cells were rinsed (once) with PBS, detached by trypsin (300 µL) and counted using the Luna machine. The counting process enabled the seeding of a precise number of cells for the next step. 200 cells were seeded in six-well plates (in sixplicates) and incubated for 7 days. When the period elapsed, cells were stained with crystal violet (1 %) in ethanol (50%) for 15 minutes. Crystal violet stained the cells while ethanol fixed them. After staining, cells were washed with water (three times) and the colonies were counted. The cells' plating efficiency (PE) was calculated with respect to the control samples using the relationship in equation 2.

$$PE = \frac{Number\ of\ colonies}{Number\ of\ cells\ seeded\ first} \qquad (2)$$

With increasing concentrations of perfluorinated micelles, the cell survival fraction was evaluated (equation 3) and a histogram was plotted to obtain the toxicity as a function of the NP concentration.

$$Survival\ fraction = \frac{Number\ of\ colonies}{(Number\ of\ cells\ seeded\ first \times PE)} \qquad (3)$$

2.6.4 Radiation assay. Radiation experiments were carried out to evaluate the radiosensitisation/radioamplification potential of AuNP@PFTD-PEG on cancer cell cultures. For this, T25 flasks were used and cells were seeded at a density of 10^5 cells

mL^{-1} (in culture medium) and allowed to adhere for 24 hours in an incubator (maintained at the same conditions previously described). After cell adhesion, the medium was discarded and cells were incubated with AuNP@PFTD-PEG at 0.25 mg mL^{-1}. For comparison, cells were also incubated with medium, PFTD-PEG micelles (0.25 mg mL^{-1}), PtNP (0.5 mM) and PtNP with PFTD-PEG micelle (in triplicates). This incubation step lasted for 24 h and once complete, the media in each T25 flask was replaced with a fresh one and the samples were ready for irradiation. Irradiation was carried out at different time periods, with a dose range from 0 to 6 Gy at 1 Gy min^{-1}, thanks to the X-ray accelerator (source) at Institute of Physical Chemistry (ICP), Paris Saclay. When irradiation was over, cells in each T25 flask were trypsinated, counted and seeded in six-well plates at different densities, ranging from 150 to 4800, considering higher irradiation doses, to ensure sufficient colony formation even at higher doses. The cells were incubated for 7 days and afterwards, they were stained with crystal violet (1 %) in ethanol (50%) for 15 min, rinsed with water (after staining) and the colonies were counted. The plating efficiency and the survival fraction were calculated as described above.

3. RESULTS AND DISCUSSION

3.1 Synthesis of PFTD-PEG amphiphile and micelle formation.

PFTD-PEG amphiphiles were synthesised according to the protocol reported by the CEA team in their article led by Jamgotchian et al[29]. This synthesis proceeded in two steps. In the first step, the hydroxyl function of PEG was activated by tosyl chloride to yield the intermediate PEG-OTs. In the second step, PEG-OTs reacted with PFSH to yield the amphiphile, PFTD-PEG by nucleophilic substitution. This amphiphilic unit has a hydrophilic head made of PEG and a hydrophobic chain comprising of fluorine atoms. The PEG polar head, with zero surface charge, has significance in preventing opsonisation of the micelle *in vivo*, thus allowing a prolonged circulation time. As a result, solid tumours are passively targeted through the EPR effect, which allows the accumulation of NP in the tumour's leaky vasculature. Due to fluorine's low polarizability, leading to weak van der Waals forces, the fluorinated chain at the core of the micelles possesses both hydrophobic and lipophobic properties, which ensure the micelles' stability *in vivo*[28].

Critical micelle concentration was determined by du Noüy-Padday method, and a value of 0.061 mg mL^{-1} was obtained. Thereafter, PFTD-PEG amphiphiles (20 mg) were added to ultra-pure water (2 mL), followed by sonication to obtain the PFTD-PEG micelle (Figure 10).

Step one

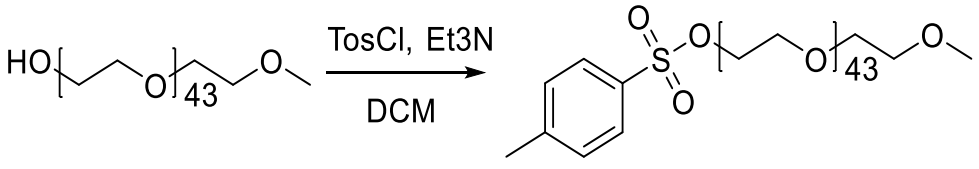

PEG PEG-OTs

PEG-OTs :

^{1}H NMR (400 MHz, $CDCl_3$): δ 7.75 (d, J = 8.3 Hz, 2H), 7.30 (d, J = 8.3 Hz, 2H), 4.12–4.10 (m, 2H), 3.78 - 3.57 (m, 174H), 3.33 (s, 3H), 2.40 ppm (s, 3H).

^{13}C NMR (100 MHz, $CDCl_3$): δ 144.8, 133.1, 129.8, 128, 72, 70.6, 69.3, 68.7, 59, 29.7, 21.6 ppm.
ESI-MS (ES+): *m/z* $[M+Na]^+$ observed:2146.1777; *m/z* $[M+Na]^+$ calculated:2146.1782

Step two

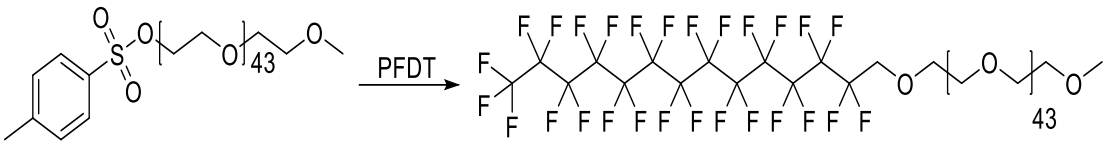

PEG-OTs PFTD-PEG

PFTD-PEG:
^{1}H NMR (400 MHz, $CDCl_3$) δ 4.04 (t, J = 13.8 Hz, 2H), 3.84–3.43 (m, 176H), 3.37 ppm (s, 3H).
^{13}C NMR (100 MHz, $CDCl_3$) δ 72.5, 72.1, 70.7, 59.1 ppm.
^{19}F NMR (376 MHz, $CDCl_3$) δ –80.7 (t, J = 10.0 Hz), –119.7 (t, J = 14.6 Hz), –121.4 to –122.1 (m), –122.6 (s), –123.4 (s), –126.0 to –126.1 ppm (m).
ESI-MS (ES+): *m/z* $[M+Na]^+$ observed: 2674.1340; *m/z* $[M+Na]^+$ calculated: 2674.1340

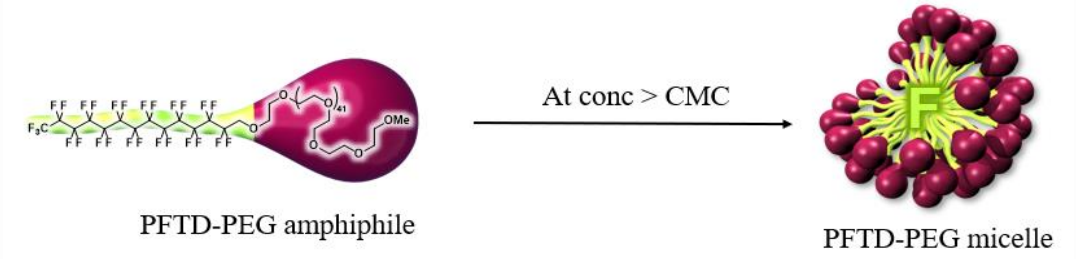

Figure 10. Formation of PFTD-PEG micelle from the amphiphilic units

3.1.1 Characterisation of micelle

Determination of micellar CMC. Critical micelle concentration represents the concentration above which amphiphiles begin to form micelles. In this case, du Noüy-Padday method was used to determine the CMC of PFTD-PEG amphiphile (Figure 11). With this method, the surface tension of the micelle solution at different concentrations was accessed. Below the CMC, amphiphiles arrange themselves at the liquid-air interface, and increasing the amphiphile concentration decreases the surface tension. At CMC, the liquid-air interface is saturated, meaning any further addition of amphiphiles results in the formation of micelles, thus the surface tension remains unchanged. In this process, the fluorinated hydrophobic tails assemble in the interior of the micelle and PEGylated hydrophilic head at its exterior. The surface tension was plotted as a function of the micelle concentration and two straight lines were obtained. Their point of intersection was estimated as the CMC, leading to a value of 0.061 mg mL^{-1}.This low CMC value has significance in biological applications, as it limits hemodilution of the micelles *in vivo*. Micelles administered *in vivo* are diluted by the blood, and if their concentration falls below the CMC, they dissociate into free amphiphiles, thereby releasing their content before reaching the desired target. Therefore, to avoid this occurrence, micelles should be designed with as low CMC values as possible[42].

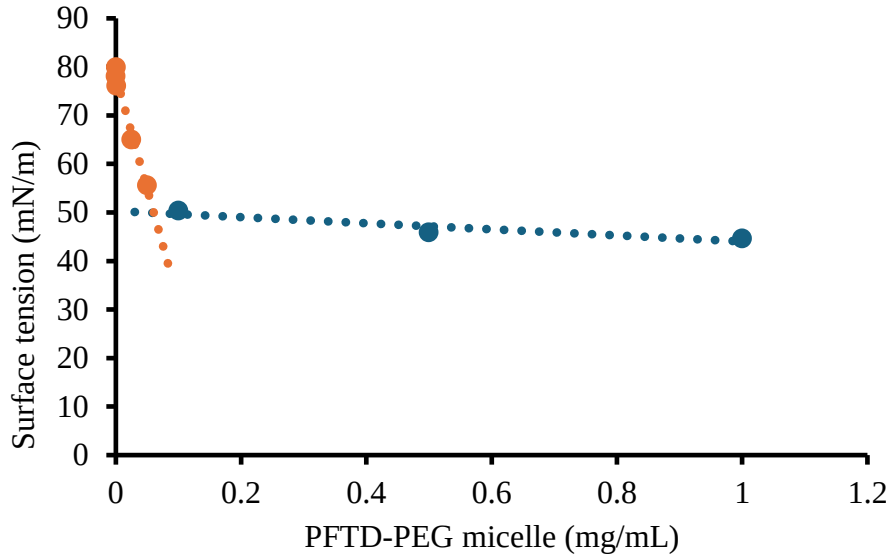

Figure 11. Determination of the critical micelle concentration of PFTD-PEG amphiphile

DLS measurements of the micelle. The hydrodynamic diameter of PFTD-PEG micelles, accessed by DLS was found to be 8.5 nm. This small micellar size, alongside its zero surface charge and low CMC value, allows the micelle's stability and easy penetration into the tumour.

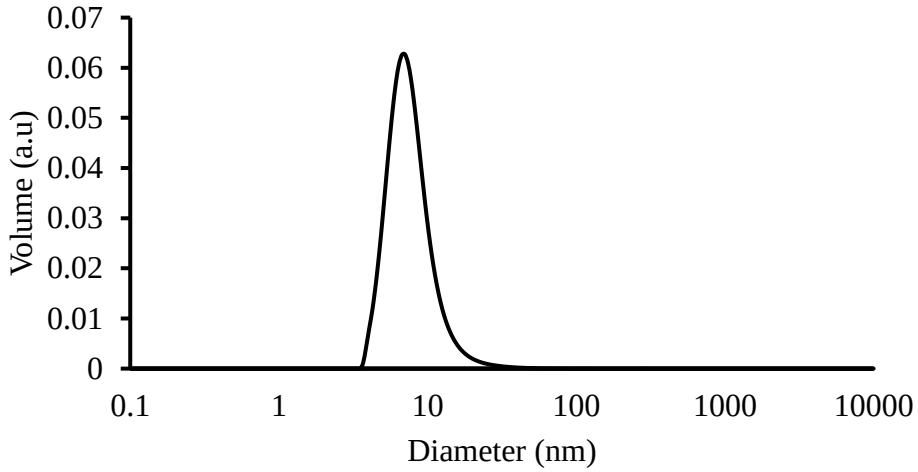

Figure 12. DLS analysis of PFTD-PEG micelle

3.2 Synthesis of Gold nanoparticles and encapsulation with micelle

The synthesis of AuNPs makes it possible to control the size, shape and surface charge. In general, this synthesis has three stages, first the chemical synthesis of the nanoparticle, followed by addition of ligand for stability and finally surface functionalisation for enhanced retention in the target tissue.

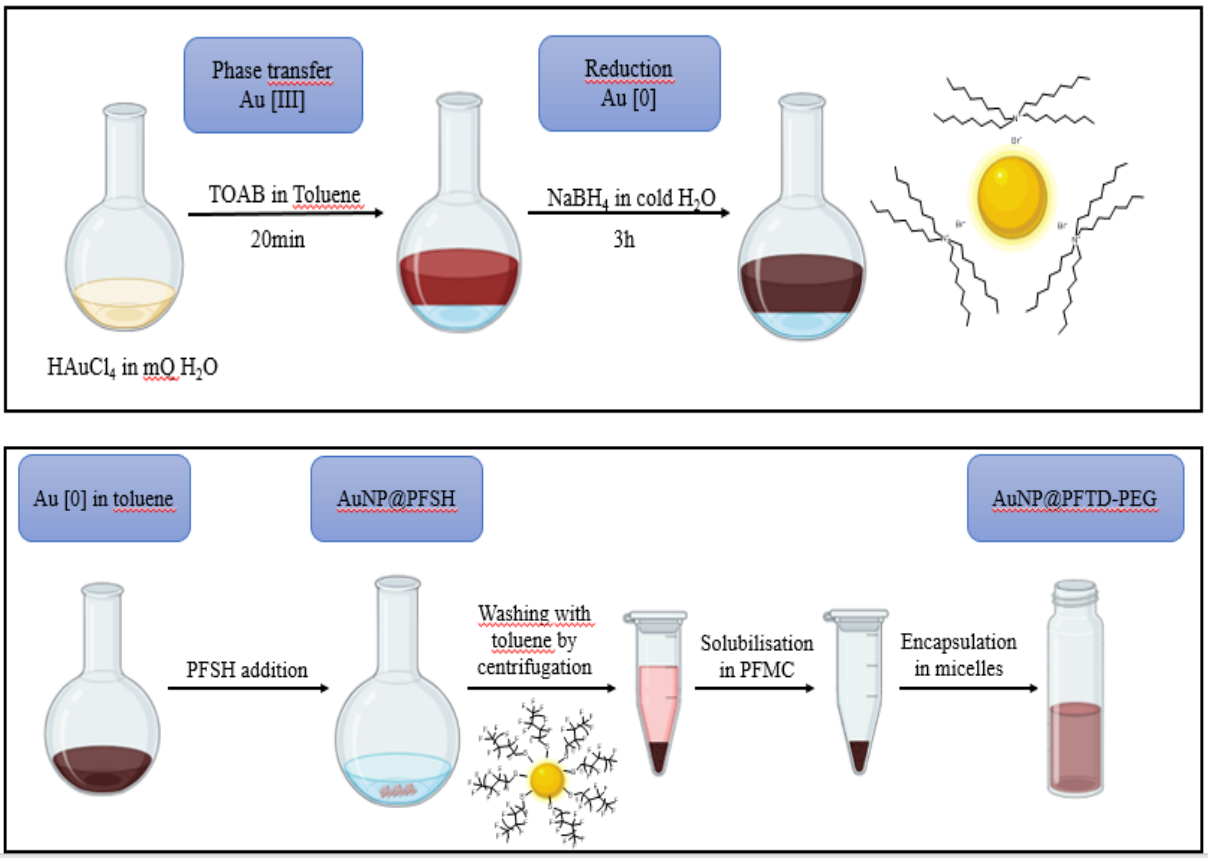

Figure 13a. Synthesis of AuNPs.

The protocol used here, which is a modification of the Brust-Schiffrin method (Figure 13) allowed the direct reduction of Au(III) to Au(0), as opposed to the Brust Schiffrin method, where the reduction of gold proceeds from Au(III) to Au(I) to Au(0)[43]. It has been shown that the formation of Au (I) species increased polydispersity in the NP size, hence the modification of the protocol to avoid this occurrence. In the modified protocol, TOAB dissolved in toluene was added to $HAuCl_4.3H_2O$ dissolved in water, resulting in a biphasic mixture. Vigorous stirring allowed a phase transfer of gold from the aqueous phase to the organic (toluene) phase, after which $NaBH_4$ was added, which reduced the gold directly from Au(III) to Au(0). This reaction was visible due to the colour change in the flask. The two phases were separated, and perfluorinated thiol (PFSH) was added to the Au-containing organic phase, to displace the TOAB and stabilise the AuNP. There was an immediate precipitation of AuNPs following this step, after which several washing/ centrifugation steps with sonication were carried out to get rid of TOAB. These AuNPs functionalised with perfluorinated ligand were only dispersable in perfluorinated solvents, thus after the washing step, they were dispersed in PFMC in order to obtain the AuNP solution.

AuNPs were then encapsulated into the micelle according to the protocol described previously to obtain AuNP@PFTD-PEG (Figure 13b).

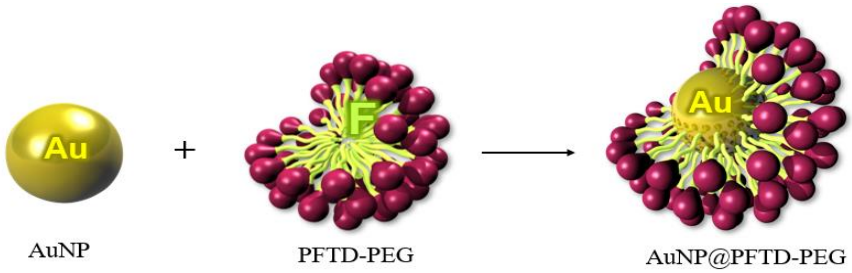

Figure 13b. Encapsulation of AuNP within PFTD-PEG micelle

3.2.1 Characterization of AuNP@PFTD-PEG

Dynamic Light Scattering. After loading the micelle with AuNP, DLS analysis (Figure 14a) reviewed an increase in the micellar size from 8.5 to 15 nm. This showed that the AuNP was well encapsulated in the micelle.

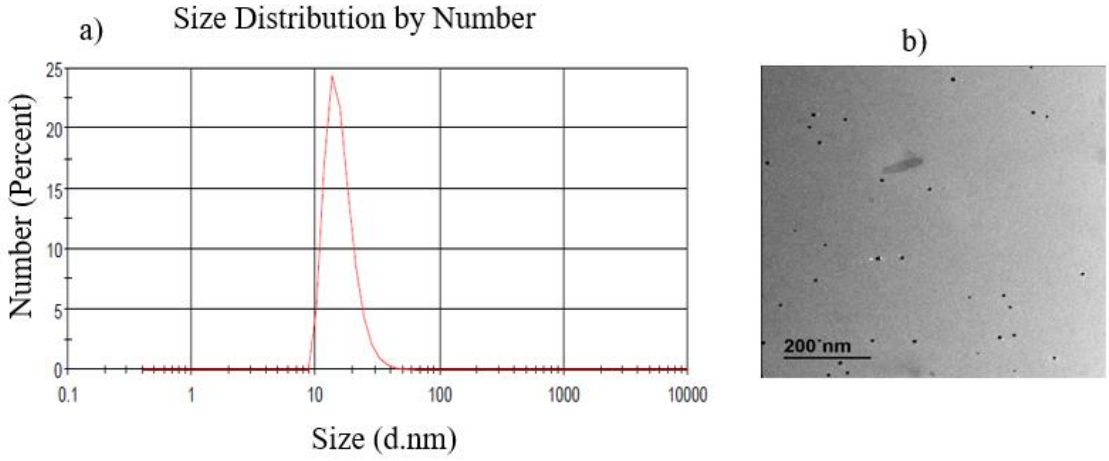

Figure 14. a) DLS and b) TEM analysis of AuNP@PFTD-PEG

Transmission Electron Microscopy. The size of AuNP@PFTD-PEG was also analysed using Transmission Electron Microscopy. TEM image analysis resulted in AuNP size of 6±1.8 nm (Figure 14b). It should be noted that since TEM leverages the material's electron density to generate an image, only the size of electron-dense AuNP was revealed. The PFTD-PEG shell, which has a low electron density, was not captured, except for its shady appearance around the AuNP. Characterisation using cryo-TEM will be most efficient in revealing the optimal size of AuNP@PFTD-PEG. However, from the DLS diameter of 8.5 nm for the PFTD-PEG micelle alone, and the AuNP size of 6 nm from TEM, this sums up the give a value of 14.5 nm for the AuNP@PFTD-PEG micelle, which agrees with the DLS measurement of 15 nm for AuNP@PFTD-PEG.

3.3 In vitro analysis of AuNP@micelle

3.3.1 Cell culture on B16F10 cells and bicarbonate buffering system. B16F10 cells, isolated from the skin tissue of mice with melanoma, are very sensitive to changes in environmental conditions[44]. Initially, these cells were cultured in an incubator at 5% CO_2 and maintained at 37 °C. The cells proliferated very fast, adapting a spindle-shaped and epithelial-like cells morphology. During the experiments, the cells started to produce melanin, changing their colour from light brown to black (Figure 15). The cells changed morphology and stopped growing, adapting a circular shape with melanin accumulation. The media colour also changed from red to pink (sign of alkalinity).

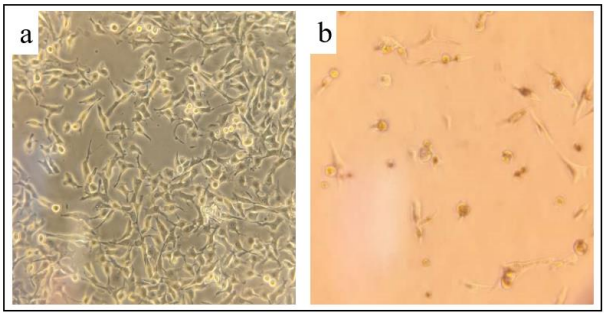

Figure 15. a) Healthy B16F10 cells with spindle-shaped and epithelial-like cells morphology; b) Abnormal B16F10 cells with accumulation of melanin.

To investigate the change in behavior of the cells, first the culture medium was checked for possible contaminations. When no contamination was found, the cells (cultured in medium containing 3.7 g/L $NaHCO_3$) were placed in three different incubators, set at 5, 7 and 10% CO_2 concentrations and the pH of each medium was measured with a pH meter and a pH paper. pH levels of about 8.5, 8 and 7.5 were observed for the respective CO_2 concentrations. It was also possible to visually access obvious pH changes in the culture media due to the presence of phenol red, which changed colour with respect to the medium pH[45].

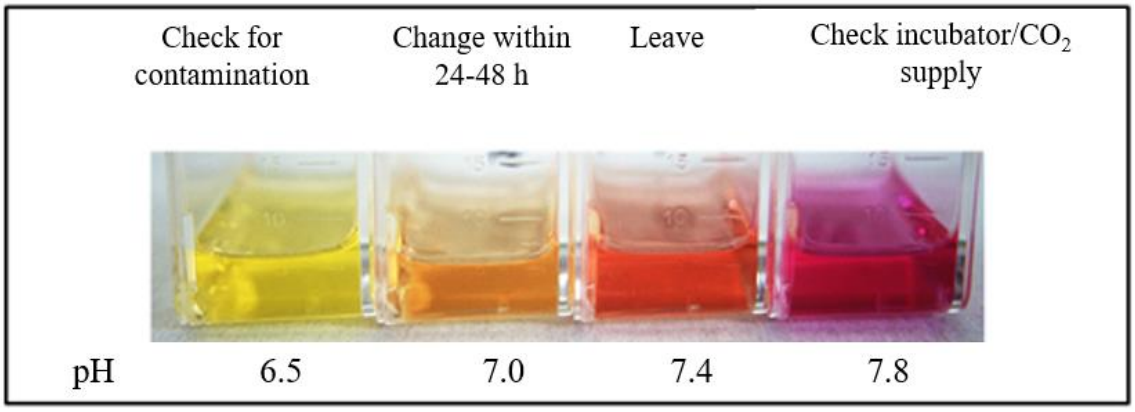

Figure 16. Media color at corresponding pH (Adapted from culturecollections.org)[45].

Since the pH of 7.5 obtained at 10 % CO_2 was closer to physiological conditions, a new vial of B16F10 cells was defreezed and incubated in culture medium at 10 % CO_2. To take additional precautionary measures, the culture flask containing the medium was placed in the incubator for a few minutes, to ensure equilibrium in pH, before adding the cells into it. As this was a friday and B16F10 cells grow very fast (doubling every 7 hours), the vial of cells was defreezed into two T175 culture flasks, ensuring enough room for cells to grow and divide during the weekend. Upon checking the cells on monday morning, it was observed that the two flasks were confluent, looking healthy with the right morphology (spindle-shaped and epithelial-like cells). The medium also maintained a reddish-orange color, which was a good indication of physiological pH, 7.4 (Figure 16)[45].

Thanks to Johanna et al[46] who illustrated the relationship between % CO_2 and the $NaHCO_3$ concentration as it relates to the pH (Figure 17). Due to physiological processes in live cell culture, pH changes are inevitable[46]. To stabilize these changes in pH, carbonic buffering system (CO_2/ HCO_3^-, equation 4) is implemented in the culture media[47].

$$H_2O + CO_2 \leftrightarrow H_2CO_3 \leftrightarrow H^+ + HCO_3^- \quad (4)$$

To achieve this buffering condition, the culture media is enriched with bicarbonate salt, $NaHCO_3$, which produces bicarbonate ions HCO_3^- (a base). On the other hand, the incubator is furnished with CO_2 which produces carbonic acid. However, when $NaHCO_3$ is in excess (more HCO_3^- present), the culture media turns alkaline. On the other hand, too high concentrations of CO_2 make the media acidic. An equilibrium between the acid and the base stabilises the buffer system. This helps to counterbalance any little changes in pH due to cellular activity, thus ensuring physiological pH in the culture media. The DMEM used (containing 3.7 g/L $NaHCO_3$) was found to be buffered for higher CO_2 concentrations, higher than the 5% CO_2 of the incubator in use. To achieve equilibrium of the buffer system, the incubator was set at 10% CO_2 when media containing 3.7 g/L $NaHCO_3$ was used. This suggests that for cells cultured in 5% CO_2 incubator, 1.5 g/L of $NaHCO_3$ will be ideal to maintain the desired physiological pH[47].

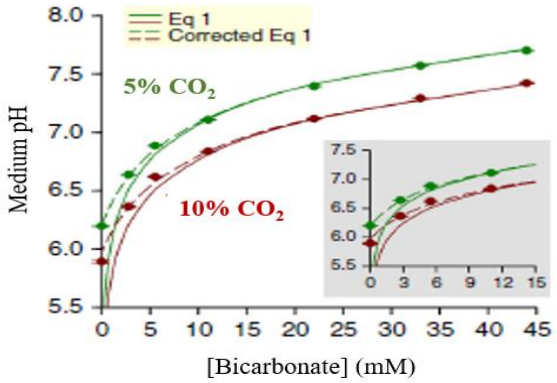

Figure 17. Relationship between bicarbonate, CO_2 and pH (Adapted from culturecollections.org)[45]

3.3.2 Confocal Microscopy Experiments. To enhance the radiation effect, AuNP@PFTD-PEG should accumulate in the tumour cells. Confocal microscopy was carried out to ascertain the internalisation of this NP in cells. It was envisioned that its internalisation would serve imaging purposes, thus helping to track the precise location of nanoparticles *in vivo*. DiD dye was encapsulated within the nanoparticle to obtain AuNPDiD@PFTD-PEG. Confocal microscopy was carried out to image the cells after internalization with AuNPDiD@PFTD-PEG. To enable visualization of the nucleus, Dapi dye was used for its staining. The red channel in Figure 18a) represents AuNPDiD@PFTD-PEG, the blue channel in Figure b) stands for the nucleus staining and Figure c) is the composite image. While the nucleus was clearly visualised, the fluorescence of the AuNPDiD@PFTD-PEG (red channel) was weak, however the NP was still visible. The weak fluorescence could be because a part of the DiD dye was not well encapsulated in the NP. This was confirmed by the precipitates of the free Did observed in the sample when left standing for a few days. Nevertheless, the visualisation of this NP *in vitro* shows its imaging potential. Currently, the CEA team is actively searching for other protocols for the encapsulation of the dye to avoid its precipitation. Assessing the encapsulation of all the Did is important, to ensure that what is being visualised is indeed the NP and not free Did and a method to achieve this is needed.

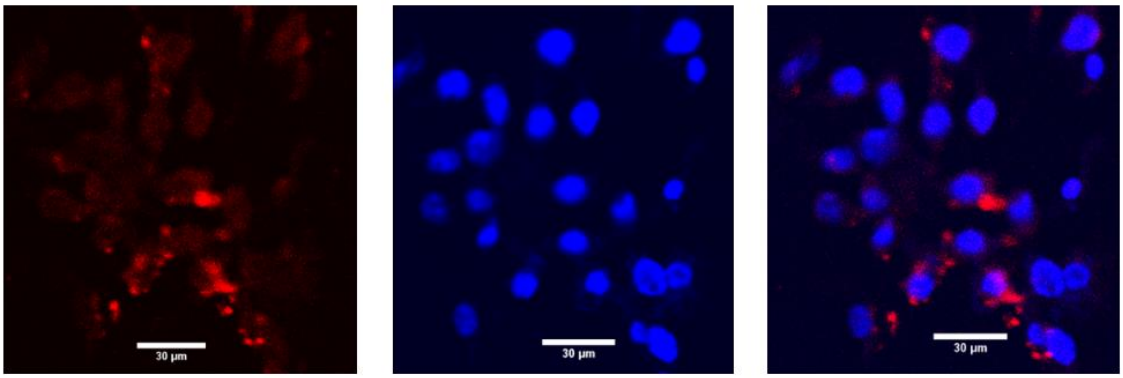

Figure 18. a) Red channel for AuNPDiD@micelle, b) Blue channel for the nucleus stained with Dapi, c) The composite image.

3.3.3 Clonogenic assay on B16F10 cells. The survival fraction of B16F10 cells in the presence of AuNP@PFTD-PEG was estimated via clonogenic assay as presented in the histogram below (Figure 19).

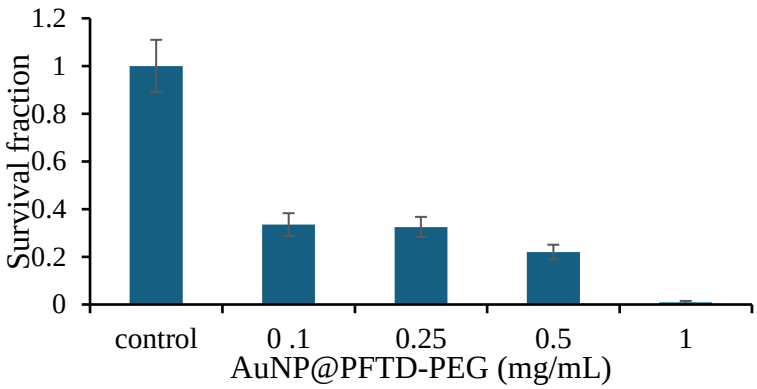

Figure 19. Clonogenic assay of AuNP@PFTD-PEG on B16F10 cells.

The result showed that AuNP@PFTD-PEG was toxic to the cells even at the least NP concentration. The survival rates at 0.1 and 0.25 mg mL^{-1} were very similar (34 and 33 % respectively). As previous experiments with the micelle proved its non-toxicity, the experienced toxicity could be due to traces of TOAB or solvent (from AuNP synthesis) that were not completely removed during the purification process.

3.3.4 Irradiation of B16F10 cells. Since the same survival rate was observed at 0.1 and 0.25 mg mL^{-1} of AuNP@PFTD-PEG, 0.25 mg mL^{-1} concentration was chosen for irradiation experiments. AuNP@PFTD-PEG and PFTD-PEG micelle alone (0.25 mg mL^{-1}) were loaded into the cells and irradiated at 0 to 6 Gy. Due to the toxicity of AuNP@PFTD-PEG, PtNPs were also used, to establish a proof of concept. Therefore, the cells were incubated with PtNPs (0.5 mM) plus PFTD-PEG micelle (0.25 mg mL^{-1}) and PtNPs alone (0.5mM). Additionally, a control sample was prepared with medium and water.

At 2 Gy (Figure 20 a), the survival fraction for the Ctrl, PFTD-PEG micelle and AuNP@ PFTD-PEG were 0.58, 0.50 and 0.30 respectively. This showed that PFTD-PEG micelles delivered oxygen to the tumour, thereby radiosensitising it, so that more cell killing is

achieved in the presence of irradiation. Therefore, micelle effect was observed as in the article [27]. There was also an evidence of additive effect due to the presence of gold in the micelle, as a lower cell survival was obtained in the composite NP. The result is very promising but the AuNP@micelle was too toxic to propose it for medical purposes, so a new formulation is in progress to improve the results.

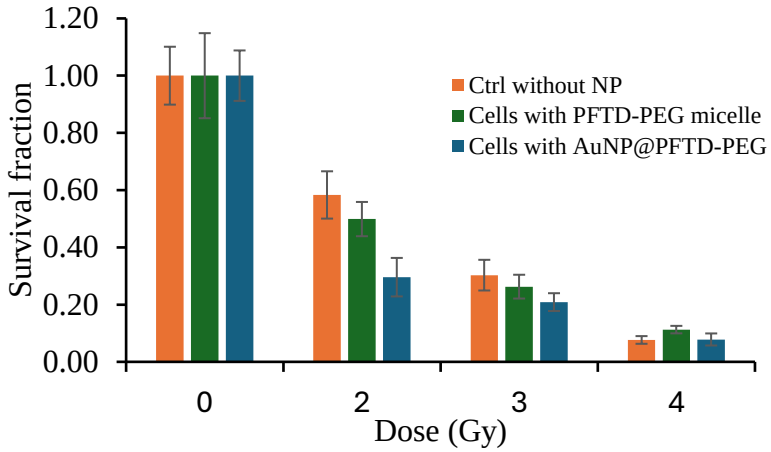

Figure 20a. Radiation assay on B16F10 cells, showing the survival fraction at different doses.

To prove the additive effect observed with AuNP@micelle, cells were also incubated with PtNPs plus PFTD-PEG micelles and PtNP alone. At 2 Gy (Figure 20 b), the survival fraction for the Ctrl, PtNPs and PtNPs plus PFTD-PEG micelles were 0.58, 0.48 and 0.43 respectively.

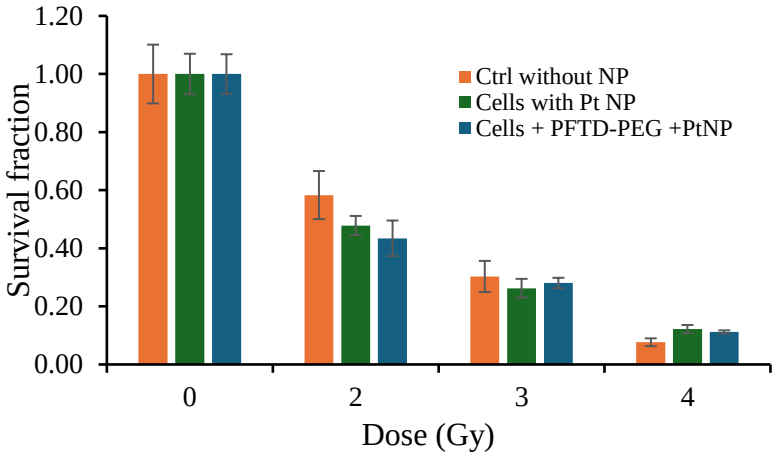

Figure 20b. Radiation assay on B16F10 cells, showing the survival fraction at different doses.

Pt NP amplified the effect of radiation, thus inducing more cell killing, which agrees with the reports from literature on the radio-amplification potential of Pt NPs[38]. Even more cell killing was achieved, when PtNP plus PFTD-PEG micelles were internalised into cells. This is due to the micelles acting like oxygen shuttles, taking it from the extracellular environment to the intracellular compartment where it interacts with irradiation and secondary electrons produced by the NPs. The PtNPs on the other hand released electrons, thereby increasing the overall number of electrons generated. These

electrons either interact directly with cells or react with oxygen to produce reactive species that cause cytotoxicity[37].

For both cases, the data points were not reliable after 4 Gy, due to high cell killing, resulting in bad statistics. The irradiation experiment was done only once in the frame of the internship and must be repeated.

4 CONCLUSION AND FUTURE PERSPECTIVES

PFTD-PEG amphiphiles were synthesised and formulated into PFTD-PEG micelles. AuNPs were synthesised according to the protocol, which is a modification of the Brust-Schiffrin method and spherical AuNPs with size 6 nm were obtained. AuNPs were further encapsulated within PFTD-PEG micelles to obtain the particle AuNP@PFTD-PEG. The idea was to evaluate the synergistic effect of this NP, with PFTD-PEG micelle as a radiosensitiser and AuNP as a radioamplifier. The internalization of this NP was confirmed by confocal microscopy, however clonogenic assay reviewed the NPs' toxicity even at the least concentration of 0.1 mg mL^{-1}. Irradiation experiments proved its radiosensitisation/radioamplification potential but since the nanocarrier (AuNP@PFTD-PEG) was confirmed toxic, irradiaton experiments were also conducted on PtNP plus PFTD-PEG micelle to access the synergistic effect of the two particles (radioamplifier/radiosensitizer) on B16F10 cancer cell cultures. Indeed, more cell killing was achieved when Pt NP and PFTD-PEG micelle were internalised together in the cells, compared to cells with Pt NP only, micelles only and the control. The effect was clearly noticed at 2 Gy, which is the most common dosage used in conventional radiotherapy.

As there were only few data points for the irradiation, it was difficult to calculate the sensitizer enhancement ratio, however, the protocol is being optimised for the next irradiation to ensure more data points. The toxicity experienced with AuNP@PFTD-PEG is assumed to come from AuNP due to incomplete purification after its synthesis, therefore, the CEA team is actively searching alternative synthetic protocols and Turkevich method is being considered. In future, it will be interesting to carry out toxicity tests for AuNPs and PFTD-PEG micelles first, before encapsulation, as this will give a clearer picture of the toxicity, whether it is coming from AuNP or it is a function of the composite NP. Apart from UV-Vis spectroscopy, a method to check that Did dye is well encapsulated in the NP will be necessary to ensure that the NP is being visualised and not the free Did. Overall, AuNP@PFTD-PEG holds promise as a nanovector in significantly enhancing the outcome of radiotherapy and a little more effort in optimising the synthesis will bring about this effect.

5 REFERENCES

1. Gianfaldoni S, Gianfaldoni R, Wollina U, Lotti J, Tchernev G, Lotti T. An Overview on Radiotherapy: From Its History to Its Current Applications in Dermatology. Open Access Maced J Med Sci. 2017 Jul 18;5(4):521-525. doi: 10.3889/oamjms.2017.122. PMID: 28785349; PMCID: PMC5535674.
2. Vaidya, J. S. (2024). Principles of cancer treatment by radiotherapy. *Surgery (Oxford)*.
3. Pina-Sanchez, P., Chavez-Gonzalez, A., Ruiz-Tachiquin, M., Vadillo, E., Monroy-Garcia, A., Montesinos, J. J., ... & Mayani, H. (2021). Cancer biology, epidemiology, and treatment in the 21st century: current status and future challenges from a biomedical perspective. *Cancer Control*, *28*, 10732748211038735.
4. Sung, H., Ferlay, J., Siegel, R. L., Laversanne, M., Soerjomataram, I., Jemal, A., & Bray, F. (2021). Global cancer statistics 2020: GLOBOCAN estimates of incidence and mortality worldwide for 36 cancers in 185 countries. *CA: a cancer journal for clinicians*, *71*(3), 209-249.
5. Mehta, S. R., Suhag, V., Semwal, M., & Sharma, N. (2010). Radiotherapy: basic concepts and recent advances. *Medical Journal Armed Forces India*, *66*(2), 158-162
6. Chalmers, M. (2003). How particle physics can be therapeutic. *Physics world*, *16*(8), 32.
7. Do Huh, H., & Kim, S. (2020). History of radiation therapy technology. *Progress in Medical Physics*, *31*(3), 124-134.
8. Mott, J. H. L., & Daniel, J. M. (2021). Interactions of Electromagnetic Radiation and Subatomic Particles with Matter-Part 1. *Clinical oncology (Royal College of Radiologists (Great Britain))*, *33*(7), 451-454.
9. Laprise-Pelletier, M., Simão, T., & Fortin, M. A. (2018). Gold nanoparticles in radiotherapy and recent progress in nanobrachytherapy. *Advanced healthcare materials*, *7*(16), 1701460.
10. Wang, H., Jiang, H., Van De Gucht, M., & De Ridder, M. (2019). Hypoxic radioresistance: can ROS be the key to overcome it?. *Cancers*, *11*(1), 112.
11. Karger, C. P., Glowa, C., Peschke, P., & Kraft-Weyrather, W. (2021). The RBE in ion beam radiotherapy: in vivo studies and clinical application. *Zeitschrift für Medizinische Physik*, *31*(2), 105-121.
12. Hullo, M., Grall, R., Perrot, Y., Mathé, C., Ménard, V., Yang, X., ... & Bourneuf, E. (2021). Radiation enhancer effect of platinum nanoparticles in breast cancer cell lines: In vitro and in silico analyses. *International Journal of Molecular Sciences*, *22*(9), 4436
13. Krafft, M. P. (2020). Alleviating tumor hypoxia with perfluorocarbon-based oxygen carriers. *Current Opinion in Pharmacology*, *53*, 117-125.
14. Stubbs, M. (2020). Hypoxia. *Southern African Journal of Anaesthesia and Analgesia*, *26*(6), S157-160.
15. Boulefour, W., Rowinski, E., Louati, S., Sotton, S., Wozny, A. S., Moreno-Acosta, P., ... & Magne, N. (2021). A review of the role of hypoxia in radioresistance in cancer therapy. *Medical science monitor: international medical journal of experimental and clinical research*, *27*, e934116-1.
16. Charolidi, N., & Carroll, V. A. (2017). Hypoxia and pulmonary hypertension. *Hypoxia Hum Dis*.
17. Krafft, M. P., & Riess, J. G. (2021). Therapeutic oxygen delivery by perfluorocarbon-based colloids. *Advances in colloid and interface science*, *294*, 102407.

18. Hatfield, S. M., & Sitkovsky, M. (2016). A2A adenosine receptor antagonists to weaken the hypoxia-HIF-1α driven immunosuppression and improve immunotherapies of cancer. *Current opinion in pharmacology*, *29*, 90-96.
19. Feldman, L. A., Fabre, M. S., Grasso, C., Reid, D., Broaddus, W. C., Lanza, G. M., ... & Herst, P. M. (2017). Perfluorocarbon emulsions radiosensitise brain tumors in carbogen breathing mice with orthotopic GL261 gliomas. *PLoS One*, *12*(9), e0184250.
20. Chattaraj, R., Blum, N. T., & Goodwin, A. P. (2019). Design and application of stimulus-responsive droplets and bubbles stabilized by phospholipid monolayers. *Current opinion in colloid & interface science*, *40*, 14-24.
21. Riess, J. G. (2005). Understanding the fundamentals of perfluorocarbons and perfluorocarbon emulsions relevant to in vivo oxygen delivery. *Artificial cells, blood substitutes, and biotechnology*, *33*(1), 47-63.
22. Riess, J. G. (2009). Highly fluorinated amphiphilic molecules and self-assemblies with biomedical potential. *Current opinion in colloid & interface science*, *14*(5), 294-304.
23. Zhou, Y., Wang, R., Teng, Z., Wang, Z., Hu, B., Kolios, M., ... & Zheng, Y. (2016). Magnetic nanoparticle-promoted droplet vaporization for in vivo stimuli-responsive cancer theranostics. *NPG Asia Materials*, *8*(9), e313-e313.
24. Ke, H., Wang, J., Tong, S., Jin, Y., Wang, S., Qu, E., Bao, G., Dai, Z. (2014). Gold Nanoshelled Liquid Perfluorocarbon Magnetic Nanocapsules: a Nanotheranostic Platform for Bimodal Ultrasound/Magnetic Resonance Imaging Guided Photothermal Tumor Ablation. Theranostics, 4(1), 12-23. https://doi.org/10.7150/thno.7275.
25. Lu, N., Fan, W., Yi, X., Wang, S., Wang, Z., Tian, R., ... & Chen, X. (2018). Biodegradable hollow mesoporous organosilica nanotheranostics for mild hyperthermia-induced bubble-enhanced oxygen-sensitized radiotherapy. *ACS nano*, *12*(2), 1580-1591.
26. Song, G., Liang, C., Yi, X., Zhao, Q., Cheng, L., Yang, K., & Liu, Z. (2016). Perfluorocarbon-loaded hollow Bi2Se3 nanoparticles for timely supply of oxygen under near-infrared light to enhance the radiotherapy of cancer. *Advanced materials (Deerfield Beach, Fla.)*, *28*(14), 2716-2723.
27. Godel-Pastre, S., Porcel, E., Pinna, G., Vandamme, M., Denis, C., Leterrier, C., ... & Gravel, E. (2024). Tumor-Targeted Perfluorinated Micelles as Efficient Theranostic Agents Combining Positron Emission Tomography and Radiosensitization. *ACS Applied Materials & Interfaces*, *16*(17), 21557-21570.
28. Jhaveri, A. M., & Torchilin, V. P. (2014). Multifunctional polymeric micelles for delivery of drugs and siRNA. *Frontiers in pharmacology*, *5*, 77.
29. Jamgotchian, L., Vaillant, S., Selingue, E., Doerflinger, A., Belime, A., Vandamme, M., ... & Doris, E. (2021). Tumor-targeted superfluorinated micellar probe for sensitive in vivo 19 F-MRI. *Nanoscale*, *13*(4), 2373-2377.
30. Pagáčová, E., Štefančíková, L., Schmidt-Kaler, F., Hildenbrand, G., Vičar, T., Depeš, D., ... & Falk, M. (2019). Challenges and contradictions of metal nano-particle applications for radio-sensitivity enhancement in cancer therapy. *International journal of molecular sciences*, *20*(3), 588.
31. Jiménez Sánchez, G., Maury, P., Stefancikova, L., Campion, O., Laurent, G., Chateau, A., ... & Roux, S. (2019). Fluorescent radiosensitizing gold nanoparticles. *International Journal of Molecular Sciences*, *20*(18), 4618.

32. George, R., Fétiveau, L., Porcel, E., Savina, F., Bapaume, C. B., Dragoe, D., ... & Catala, L. (2023). Ultra-small platinum-based coordination nanoparticles for radiotherapy. *Materials Advances*, *4*(21), 5314-5323.
33. Hainfeld, J.F.; Slatkin, D.N.; Smilowitz, H.M. The use of gold nanoparticles to enhance radiotherapy in mice. Phys. Med. Biol.2004, 49, N309–N315.
34. Alhussan, A., Bozdoğan, E. P. D., & Chithrani, D. B. (2021). Combining gold nanoparticles with other radiosensitizing agents for unlocking the full potential of cancer radiotherapy. *Pharmaceutics*, *13*(4), 442
35. Schuemann, J., Bagley, A. F., Berbeco, R., Bromma, K., Butterworth, K. T., Byrne, H. L., ... & Krishnan, S. (2020). Roadmap for metal nanoparticles in radiation therapy: Current status, translational challenges, and future directions. *Physics in Medicine & Biology*, *65*(21), 21RM02.
36. Salado-Leza, D., Traore, A., Porcel, E., Dragoe, D., Muñoz, A., Remita, H., ... & Lacombe, S. (2019). Radio-enhancing properties of bimetallic Au: Pt nanoparticles: experimental and theoretical evidence. *International Journal of Molecular Sciences*, *20*(22), 5648.
37. Li, S., Porcel, E., Remita, H., Marco, S., Réfrégiers, M., Dutertre, M., ... & Lacombe, S. (2017). Platinum nanoparticles: An exquisite tool to overcome radioresistance. *Cancer nanotechnology*, *8*, 1-15.
38. Porcel, E., Liehn, S., Remita, H., Usami, N., Kobayashi, K., Furusawa, Y., ... & Lacombe, S. (2010). Platinum nanoparticles: a promising material for future cancer therapy?. *Nanotechnology*, *21*(8), 085103.
39. Ref. https://www.cordouan-tech.com/nanoparticle-size-dynamic-light-scattering/
40. CEA document on Transition Electron Microscopy (TEM)
41. https://ebrary.net/37808/engineering/fundamentals_confocal_laser_scanning_microscopy
42. Kapse, A., Anup, N., Patel, V., Saraogi, G. K., Mishra, D. K., & Tekade, R. K. (2020). Polymeric micelles: A ray of hope among new drug delivery systems. In *Drug Delivery Systems* (pp. 235-289). Academic Press.
43. Brust, M., Walker, M., Bethell, D., Schiffrin, D. J., & Whyman, R. (1994). Synthesis of thiol-derivatised gold nanoparticles in a two-phase liquid–liquid system. *Journal of the Chemical Society, Chemical Communications*, (7), 801-802.
44. Overwijk, W. W., & Restifo, N. P. (2000). B16 as a mouse model for human melanoma. *Current protocols in immunology*, *39*(1), 20-1.
45. https://www.culturecollections.org.uk/culture-collection-news/co2-concentration-and-ph-control-in-the-cell-culture-laboratory/
46. Michl, J., Park, K.C. & Swietach, P. Evidence-based guidelines for controlling pH in mammalian live-cell culture systems. *Commun Biol* **2**, 144 (2019). https://doi.org/10.1038/s42003-019-0393-7
47. https://cellculturedish.com/cell-culture-basics-stem-cell-media-the-what-and-why/